Title

Fast dynamic electron paramagnetic resonance (EPR) oxygen imaging using low-rank tensors

Authors

Christodoulou, Anthony G
Redler, Gage
Clifford, Bryan
et al.

Publication Date

2016-09-01

DOI

10.1016/j.jmr.2016.07.006

Peer reviewed

HHS Public Access

Author manuscript

J Magn Reson. Author manuscript; available in PMC 2017 September 01.

Published in final edited form as:

J Magn Reson. 2016 September ; 270: 176–182. doi:10.1016/j.jmr.2016.07.006.

Fast Dynamic Electron Paramagnetic Resonance (EPR) Oxygen Imaging Using Low-Rank Tensors

Anthony G. Christodoulou[1,2], **Gage Redler**[1,3], **Bryan Clifford**[1,2], **Zhi-Pei Liang**[1,2], **Howard J. Halpern**[1,3], and **Boris Epel**[1,3]

[1]Center for EPR Imaging *In Vivo* Physiology, University of Chicago, Chicago, IL 60637, USA

[2]Department of Electrical and Computer Engineering and Beckman Institute for Advanced Science and Technology, University of Illinois at Urbana-Champaign, Urbana, Illinois 61801, USA

[3]Department of Radiation and Cellular Oncology, University of Chicago, Chicago, IL 60637, USA

Abstract

Hypoxic tumors are resistant to radiotherapy, motivating the development of tools to image local oxygen concentrations. It is generally believed that stable or chronic hypoxia is the source of resistance, but more recent work suggests a role for transient hypoxia. Conventional EPR imaging (EPRI) is capable of imaging tissue pO_2 *in vivo*, with high pO_2 resolution and 1 mm spatial resolution but low imaging speed (10 min temporal resolution for T_1-based pO_2 mapping), which makes it difficult to investigate the oxygen changes, e.g. transient hypoxia. Here we describe a new imaging method which accelerates dynamic EPR oxygen imaging, allowing 3D imaging at 2 frames per minute, fast enough to image transient hypoxia at the "speed limit" of observed pO_2 change. The method centers on a low-rank tensor model that decouples the tradeoff between imaging speed, spatial coverage/resolution, and number of inversion times (pO_2 accuracy). We present a specialized sparse sampling strategy and image reconstruction algorithm for use with this model. The quality and utility of the method is demonstrated in simulations and *in vivo* experiments in tumor bearing mice.

Graphical abstract

Corresponding Author: Boris Epel, Ph.D., Center for EPR Imaging in Vivo Physiology, The University of Chicago, Department of Radiation and Cellular Oncology, MC1105, Rm: ESB-05, 5841 S. Maryland Avenue, Chicago, IL 60637, USA. bepel@uchicago.edu; Tel. +1(773)834-1938; Fax: +1(773)702-5940.

A.G.C. is now with the Cedars-Sinai Heart Institute and Biomedical Imaging Research Institute, Cedars-Sinai Medical Center, Los Angeles, CA 90048, USA

G.R. is now with the Department of Radiation Oncology, Rush University Medical Center, Chicago, IL 60612, USA

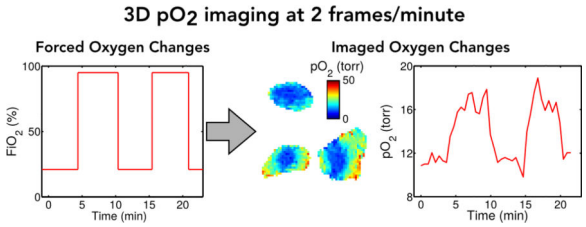

Keywords

EPR; Imaging; Oxygen; Sparse Sampling

INTRODUCTION

The importance of the oxygenation status of tumors has been known for decades [1]. Tumors with chronic hypoxia, or chronically low oxygen concentration (pO_2), show greater radiation resistance [2, 3]. This has been correlated with radiotherapy treatment failure in humans [4], leading to immense interest in methods for measuring and a fortiori imaging pO_2 deep in tissues [5].

Chronic hypoxia was the first form of hypoxia demonstrated in tumors [6]. For many years, this was thought to be the only type of hypoxia present in tumors. Brown et al. found that perfusion limited or transient hypoxia may be present as well [7–10]. However, no definitive conclusions have been made concerning the relative biologic importance of transient hypoxia relative to those of chronic hypoxia. Furthermore, lack of data correlating a quantitative measure of transient hypoxia *in vivo* with treatment outcome currently precludes such a comparison [11]. If there is significant change in the oxygenation of tumor subregions, this would argue strongly against radiation therapy that is focused on targeting radiation-resistant hypoxic areas and avoiding radiation sensitive normoxic areas based on static pO_2 images, as oxygen becomes a moving target.

Electron paramagnetic resonance imaging (EPRI) is a robust method for imaging tissue pO_2 *in vivo*. EPRI produces noninvasive 3D images of absolute pO_2 *in vivo*, highly-resolved, both spatially (~1 mm^3 voxels) and in pO_2 (1–3 torr) [12–16]. The EPR relaxation constants T_1 and T_2 are both inversely proportional to local pO_2; by collecting multiple images with different T_1- or T_2-weightings, the relaxation constant (and therefore pO_2) can be quantified [17, 18]. T_1 is an especially attractive contrast mechanism, as it reduces spin probe concentration–dependent self-broadening, which confounds T_2 based aqueous pO_2 measurements and images. T_1-based pO_2 EPRI in small animals can be obtained in 10 minutes, useful for studying chronic hypoxia. To study transient hypoxia, dynamic EPRI must be accelerated beyond its current 10 minute time-scale, without sacrificing accuracy.

Different approaches have been undertaken to accelerate EPRI. A straightforward approach of trading spatial resolution for imaging speed was used by Yasui et al [19]. Subramanian et al. accelerated data acquisition using rotating gradients [20]. Redler et al. traded signal-to-noise ratio (SNR) for imaging speed (1.5 min temporal resolution for T_1-based pO_2

imaging), and used principal component analysis as an intelligent denoising technique to observe pO_2 fluctuations in a mouse tumor [21].

Similar imaging speed challenges have been overcome in the field of MRI through the use of sparse sampling. These methods leverage natural properties of images (such as sparsity [22, 23], low-rankness/partial separability [24–26], or both [27, 28]) to reduce sampling requirements, resulting in high acceleration factors. EPR images exhibit many of the same natural properties—for example, partial separability has been exploited for signal denoising [21], and sparsity has been exploited to accelerate static EPRI [29]—but the benefits of sparse sampling for dynamic EPR oxygen imaging have yet to be explored.

In this paper, we propose a sparse sampling method exploiting low-rank tensor properties [26, 30– 32] of EPR oxygen images. This approach specifically exploits both the partial separability of space and time in EPR oxygen images (i.e., the correlation between images at different times) [21] and the partial separability of space and sequence parameters (i.e., the correlation between images with different contrast weightings) [33, 34]. In leveraging these properties, 3D *in vivo* EPR pO_2 imaging becomes possible at a 30-second time-scale, opening the door for non-invasive studies investigating transient hypoxia to eventually help determine its biological implications.

MATERIALS AND METHODS

Image Model

In order to perform dynamic pO_2 mapping, we first obtain dynamic images with multiple quantitative contrast weightings [21]. Multiple pO_2 measurement techniques are available. One example is T_1-contrast imaging, which uses a delay after an inversion preparation pulse [18]. In this case, to perform multi-contrast dynamic imaging is to measure $\rho(\mathbf{r}, t, T_I)$, a multidimensional function of spatial location $\mathbf{r}$, time t, and time after an inversion pulse T_I. This multidimensional image has prohibitively high data acquisition requirements, leading to an unsatisfactory balance of the direct tradeoffs between signal-to-noise ratio (SNR), spatial coverage/resolution, imaging speed, and the number of inversion time measurements.

In order to reduce data acquisition requirements, we propose to leverage the correlation of EPR signals across: a) space, b) time, and c) contrast weightings. First, inter- and intra-tissue signal correlation ensures that the family of (t, T_I)-signals at $N_\mathbf{r}$ different voxels, $\{\rho(\mathbf{r}_n, t, T_I)\}_{n=1}^{N_r}$, is linearly dependent, and can therefore be expressed as linear combinations of $L < N_\mathbf{r}$ template signals $\{\psi_\ell(t, T_I)\}_{\ell=1}^{L}$ with combination weights $\{u_\ell(\mathbf{r})\}_{\ell=1}^{L}$. L is small in many practical imaging scenarios, such as when there are only a few tissue types being imaged or when multiple tissues experience oxygen changes with similar timings. Second, the similarity of images across time ensures that the family of multi-contrast images at N_t different times, $\{\rho(\mathbf{r}, t_n, T_I)\}_{n=1}^{N_t}$, is also linearly dependent, expressible as linear combinations of $M < N_t$ template multi-contrast images $\{\varphi_m(\mathbf{r}, T_I)\}_{m=1}^{M}$ with combination weights $\{\nu_m(t)\}_{m=1}^{M}$. M can be particularly small when the morphology is static over time, e.g., when image dynamics arise from oxygen changes

rather than from motion, although this is not a requirement. Finally, the similarity of images with different contrast weightings ensures that the family of dynamic images with N_I different contrast weightings, $\left\{\rho\left(\mathbf{r},t,T_{1,n}\right)\right\}_{n=1}^{N_I}$, is linearly dependent and expressible as linear combinations of $N < N_I$ template dynamic images $\{\phi_n(\mathbf{r},t)\}_{n=1}^{N_I}$ with combination weights $\{w_n(T_1)\}_{n=1}^{N}$. EPR physics dictates that inversion recovery takes an exponential form; this common recovery shape inherently keeps N small by ensuring that recovery curves are correlated across many tissue types and oxygen states. Note that the "combination weights" $\{u_\ell(\mathbf{r})\}_{\ell=1}^{L}$, $\{\nu_m(t)\}_{m=1}^{M}$, and $\{w_n(T_1)\}_{n=1}^{N}$ can also be seen as template functions of space, time, and inversion time, respectively.

We exploit the correlation across each dimension by modeling $\rho(\mathbf{r}, t, T_I)$ as a low-rank tensor:

$$\rho(\mathbf{r},t,T_1)=\sum_{\ell=1}^{L}\sum_{m=1}^{M}\sum_{n=1}^{N}c_{\ell mn}u_\ell(\mathbf{r})\nu_m(t)w_n(T_1), \quad (1)$$

or equivalently,

$$\rho(\mathbf{r},t,T_1)=\sum_{\ell=1}^{L}u_\ell(\mathbf{r})\psi_\ell(t,T_1), \quad (2)$$

where

$$\psi_\ell(t,T_1)=\sum_{m=1}^{M}\sum_{n=1}^{N}c_{\ell mn}\nu_m(t)w_n(T_1). \quad (3)$$

The low-rank tensor model is named as such because the discrete elements of $\rho(\mathbf{r}, t, T_I)$ can be shaped as a 3-dimensional array (i.e., as a 3-way *tensor*) with $\mathbf{r}$, t, and T_I indexed along the first through third dimensions, respectively. The rank of this tensor is described by the model orders L, M, and N, so the tensor is *low-rank* when L, M, and N are smaller than the number of voxels, time points, and contrast weightings, respectively (which follows from the previously described properties of linear dependence).

With the proposed image model, it becomes unnecessary to collect a full set of image projections for each contrast weighting at each point in time. Data acquisition can instead be accelerated, performing image reconstruction from sparsely sampled projections. This is possible because the low-rank tensor model reduces the degrees of freedom in $\rho(\mathbf{r}, t, T_I)$, thereby reducing the number of measured data points required to determine the image. Furthermore, by decomposing the image into template functions $\{u_\ell(\mathbf{r})\}_{\ell=1}^{L}$, $\{\nu_m(t)\}_{m=1}^{M}$, and $\{w_n(T_1)\}_{n=1}^{N}$ and the small core tensor $\{c_{\ell mn}\}_{\ell=1,m=1,n=1}^{L,M,N}$, this image model decouples

the tradeoff between imaging speed, spatial coverage/resolution, and number of inversion time measurements. Consider the example of adding a time point t_0 to the image function: without the model, this requires determination of the $N_{\mathbf{r}}N_{\mathrm{I}}$ new unknowns in $\rho(\mathbf{r}, t_0, T_{\mathrm{I}})$; with the proposed model, it only requires determination of the M new unknowns in $\{\nu_m(t)\}_{m=1}^{M}$ (assuming the images at t_0 are not so uncorrelated to images at the other time points as to require a model order increase). This ability to construct $\rho(\mathbf{r}, t, T_{\mathrm{I}})$ by separately determining each individual template function and the core tensor motivates a specific data acquisition strategy designed to exploit the decoupling of conventional tradeoffs.

Data Acquisition

Sampling Strategy—Specifically focusing on the model as formed in Eq. (2), we can see that $\rho(\mathbf{r}, t, T_{\mathrm{I}})$ is constructed from two sets of functions $\{u_\ell(\mathbf{r})\}_{\ell=1}^{L}$ and $\{\psi_\ell(t, T_{\mathrm{I}})\}_{\ell=1}^{L}$. Therefore, we perform interleaved acquisition of two data sets: one appropriate for determining $\{\psi_\ell(t, T_{\mathrm{I}})\}_{\ell=1}^{L}$ and the other appropriate for determining $\{u_\ell(\mathbf{r})\}_{\ell=1}^{L}$. The first set of data—the navigator data—are auxiliary data comprising only a few projection angles cycled through at a high temporal sampling rate; these data are used to determine $\{\psi_\ell(t, T_{\mathrm{I}})\}_{\ell=1}^{L}$. The second data set—the imaging data—comprises the full set of projections, satisfying spatial resolution and field-of-view (FOV) requirements; these data, in conjunction with $\{\psi_\ell(t, T_{\mathrm{I}})\}_{\ell=1}^{L}$, will be used to recover $\{u_\ell(\mathbf{r})\}_{\ell=1}^{L}$. This sampling strategy and the model in Eq. (2) take advantage of the decoupled resolution requirements provided by low-rank tensor imaging: the reconstructed dynamic EPR image has the frame rate and T_{I}-coverage of the navigator data but the spatial resolution/FOV of the imaging data.

Imager and acquisition parameters—A pulse 250 MHz imager [13] was enhanced with a passive transmit-receive switch [35] and pulse modulator enabling π/2- and π- pulses of equal duration/bandwidth [36]. The imager was controlled with SpecMan4EPR v. 2.1 (FeMi Instruments, Chicago, IL) [37]. An inversion recovery electron spin echo (IRESE) pulse sequence with π/2- and π-pulses of 55 ns and 16 step phase CYCLOPS was used [38], as illustrated in Fig. 1. The system frequency band-pass function for each acquisition technique was measured using zero gradient sample signal amplitude at 50 spanning B_0 fields [13]. Projections were normalized using this function.

Seven images with T_{I} values from 430 ns to 5.5 μs were acquired. For accurate R_1 determination, an eighth image recorded at infinite recovery time $T_{\mathrm{I}} = \infty$ was equated to an image recorded without an inversion pulse. For voxel intensity fitting to an exponential recovery function, a $T_{\mathrm{I}} = 36$ μs was assigned to this image.

The gradient sequence used to generate the results in this paper was chosen according to an equal solid angle scheme with 18 azimuthal and polar angles and 7.5 mT/m gradient. Imaging projections were ordered using maximally spaced projection sequencing (MSPS) [39]; the navigator projections were chosen as the first 5 projections in the MSPS sequence. Acquisition of imaging and navigator projections was interleaved as shown in Fig. 2. In addition, baseline readouts were acquired every 4 projections to suppress trace artifacts, resulting in an overall sampling pattern of 520 projections acquired over the course of 23

minutes. When capturing oxygen oscillation over longer periods of time, this 23-minute imaging protocol was repeated multiple times without interscan delay.

Animal and spin probe—FSa fibrosarcomas were grown on the legs of 6–8-week-old C3H mice (HSD, Indianapolis, IN). The anesthetized animal was immobilized with a partial circumference vinyl polysiloxane cast (GC Dental Products, Kasugai, Japan) [40]. OX063 was injected IV 0.56 mmol/kg followed by infusion at 0.63 mmol/kg/hr. Tumor was defined by T_2 enhancement in RARE MRI registered with EPR images [15]. The spin probe used was the partially deuterated trityl OX063 radical methyl-tris[8-carboxy-2,2,6,6-tetrakis[2-hydroxyethyl]benzo[1,2-d:4,5-d']bis[1,3]dithiol-4-yl]-trisodium salt.

Animal experiments followed USPHS policy, and were approved by the Institutional Animal Care and Use Committee.

Image Reconstruction

Image reconstruction follows a two-step process wherein $\{\psi_\ell(t,T_I)\}_{\ell=1}^{L}$ is extracted from the navigator data and then fit to the imaging data to recover $\{u_\ell(\mathbf{r})\}_{\ell=1}^{L}$.

To define $\{\psi_\ell(t,T_I)\}_{\ell=1}^{L}$, we extract $\{\nu_m(t)\}_{m=1}^{M}$ and $\{w_n(T_I)\}_{n=1}^{N}$ from the navigator data as follows. The (**k**, t, T_I)-space navigator data are reshaped into two Casorati matrices: $\mathbf{C}_1$, the columns of which index t, and the rows of which index the available (**k**, T_I)-pairings; and $\mathbf{C}_2$, the columns of which index T_I, and the rows of which index the available (**k**, t)-pairings. Singular value decomposition (SVD) or principal component analysis (PCA) of these Casorati matrices reveals the underlying template functions: the M most significant right singular vectors of $\mathbf{C}_1$ are the template functions $\{\nu_m(t)\}_{m=1}^{M}$, and the N most significant right singular vectors of $\mathbf{C}_2$ are the template functions $\{w_n(T_I)\}_{n=1}^{N}$. M and N can be chosen from the singular value curves of $\mathbf{C}_1$ and $\mathbf{C}_2$, respectively.

Equation (3) defines $\{\psi_\ell(t,T_I)\}_{\ell=1}^{L}$ in terms of $\{\nu_m(t)\}_{m=1}^{M}$ and $\{w_n(T_I)\}_{n=1}^{N}$ (both of which are known from the navigator data) as well as the model order L and the core tensor $\{c_{\ell mn}\}_{\ell=1,m=1,n=1}^{L,M,N}$. Without knowledge of L or the core tensor, we can still define $\hat{L} = MN$ functions $\hat{\psi}_\ell(t, T_I) = \hat{\psi}_{m,n}(t, T_I) = \nu_m(t)w_n(T_I)$, where $\ell = (m-1)N + n$ indexes the Cartesian set of (m, n)-pairings. The resulting functions $\left\{\hat{\psi}_\ell(t,T_I)\right\}_{\ell=1}^{\hat{L}}$ span a tensor-product subspace containing the subspace spanned by $\{\psi_\ell(t,T_I)\}_{\ell=1}^{L}$—in other words, any linear combination of the unknown $\{\psi_\ell(t,T_I)\}_{\ell=1}^{L}$ is also a linear combination of the known $\left\{\hat{\psi}_\ell(t,T_I)\right\}_{\ell=1}^{\hat{L}}$—and are therefore fully capable of representing the desired image according to

$$\rho(\mathbf{r},t,T_I)=\sum_{\ell=1}^{\hat{L}}\hat{u}_\ell(\mathbf{r})\hat{\psi}_\ell(t,T_I). \quad (4)$$

In order to recover $\{\hat{u}_\ell(\mathbf{r})\}_{\ell=1}^{\hat{L}}$ from the imaging data, we fit the known $\left\{\hat{\psi}_\ell(t,T_1)\right\}_{\ell=1}^{\hat{L}}$ to the measured imaging projections:

$$\{\hat{u}_\ell(\mathbf{r})\}_{\ell=1}^{\hat{L}}=\arg\min_{\{\hat{u}_\ell(\mathbf{r})\}_{\ell=1}^{\hat{L}}}\left\|\mathbf{d}-\Omega\left(\sum_{\ell=1}^{\hat{L}}\mathscr{R}\{u_\ell(\mathbf{r})\}\hat{\psi}_\ell(t,T_1)\right)\right\|_2^2+\Phi(\{u_\ell(\mathbf{r})\}_{\ell=1}^{\hat{L}}), \quad (5)$$

where **d** is the vector of measured data (already inverse-Fourier-transformed from **k**-space to the projection space), $\mathscr{R}$ is the Radon transform, and Ω is the sparse sampling operator (which retains only those projections that were actually measured at each time point). The final term Φ is an optional regularization penalty. No regularization was used to generate the results in this paper, but a carefully chosen Φ could be used to enforce additional complementary image models. Numerous optimization algorithms are available to solve Eq. (5); for the purposes of this paper, we solved the unregularized quadratic optimization problem using the conjugate gradient method.

After determining $\left\{\hat{\psi}_\ell(t,T_1)\right\}_{\ell=1}^{\hat{L}}$ and $\{\hat{u}_\ell(\mathbf{r})\}_{\ell=1}^{\hat{L}}$, we obtain ρ(**r**, *t*, T_1) according to Eq. (4). Amplitude and T_1 values were fit from the recovered image; voxels with amplitude less than 15% maximum were eliminated (thresholded) from display. Image reconstruction and analysis were both performed on a workstation with dual hex-core 3.47 GHz Intel Xeon X5690 CPUs and 96 GB of RAM using in-house software written using MATLAB (Mathworks, Inc., Natick, MA).

RESULTS

Simulations

To numerically validate the proposed method, we employed an analytical phantom featuring dynamic pO_2 changes. The 3D phantom depicts seven spheres contained within a larger sphere; the smaller spheres have the same initial pO_2, with one sphere experiencing an instantaneous change in pO_2 halfway through the simulation. We compared two imaging methods: 1) the conventional sliding window method (zero-order temporal interpolation), wherein each image is reconstructed from the 80 projections nearest in time; and 2) the proposed method, wherein images are reconstructed from the full set of 208 imaging projections using the $\hat{L}$ = 4, M = 2, N = 2 temporal/inversion-recovery tensor-product subspace estimated from navigator data.

Figure 3 shows slices from pO_2 maps at four time points, as well as the pO_2 over time at a voxel in the region of interest. Images and pO_2 curves are shown from: a) the original analytical phantom; b) the sliding window reconstruction; and c) our accelerated imaging scheme using low-rank tensors. The first and last 40 frames of the sliding window reconstruction are invalid due to insufficient data to fit the window length, and are not depicted in the pO_2 time curve. The proposed method depicts the full experiment length.

In vivo experiments

In vivo pO_2 fluctuations were induced in the mouse by alternating between inhalation of two gases with different fraction of inspired oxygen (FiO_2). The normal-oxygen supply had FiO_2 = 21%; the high-oxygen supply had FiO_2 = 95% and $FiCO_2$ = 5%. Gas intake was toggled between the normal- and high-oxygen supplies at irregular intervals unknown to the imaging method. Inhaling of the $O_2 - CO_2$ mixture enhances the blood flow and increases O_2 supply to tissues [41]. Reconstruction and analysis were performed as previously described, using model order parameters $\hat{L} = 6$, $M = 3$, and $N = 2$ (chosen from the singular value curves of $\mathbf{C}_1$ and $\mathbf{C}_2$).

Figure 4 shows results from a 23-minute experiment, depicting: a) slices from 3D pO_2 maps during low-oxygen intake ($t = 2.7$ min) and high-oxygen intake ($t = 8.2$ min), with dashed lines over the axial slices denoting approximate isoparametric curves at $pO_2 = 20$; and b) the pO_2 variation over time at a voxel in the tumor periphery. Image reconstruction according to Eq. (5) took 38 minutes to complete 20 conjugate gradient iterations. Figure 5 shows results from a 115-minute experiment (i.e., by running the imaging protocol five times), depicting: a) slices from 3D pO_2 maps in a high-oxygen state ($t = 79.4$ min) and a low-oxygen state ($t = 105.1$ min), and b) the pO_2 variation over time at voxels in three tissues: muscle, the tumor periphery, and the tumor core. Image reconstruction according to Eq. (5) took 189 minutes to complete 20 conjugate gradient iterations. The frame rate of both reconstructions is 2 frames/min (i.e., a 30-second time-scale), matching the temporal sampling rate of the navigator projections.

DISCUSSION

Figure 3 demonstrates the image quality achievable by the different imaging methods. The sliding window results exhibit both strong streaking artifacts due to incomplete sampling and temporal blurring. Any attempt to fix one flaw by adjusting the window length would worsen the other: decreasing the window length would result in additional streaking artifacts, whereas increasing the window length would result in additional temporal blurring. In contrast, the proposed method is able to represent both the spatial distribution and temporal variation of pO_2 with greatly improved fidelity, having leveraged the low-rank tensor model to decouple the tradeoff between temporal blurring and streaking artifacts. Both methods underestimate the highest pO_2 value to a similar degree, but only the proposed method clearly identifies the spatiotemporal locations of the change in pO_2.

Figure 4 demonstrates the ability of the proposed imaging method to capture the pO_2 changes induced by the FiO_2 toggling experiment. The region of low pO_2 clearly visualizes the tumor, and the 30-second time-scale enables observation of the relationship between FiO_2 and pO_2, with pO_2 changes occuring within minutes of changes in FiO_2. The change in the size and location of the isoparametric curve at $pO_2 = 20$ torr (i.e., the estimated curve separating voxels with pO_2 below 20 torr from voxels with pO_2 above 20 torr) in Fig. 4(a) and the pO_2 curve in Fig. 4(c) further demonstrate the change in pO_2.

Figure 5 demonstrates the ability of our method to characterize pO_2 dynamics. For example, the experiment reveals that pO_2 level alone is not always enough to differentiate the

chronically hypoxic and possibly necrotic core of the tumor from the tumor periphery: in the low-oxygen state, the pO_2 difference between the tumor periphery and core are sometimes too small to detect. However, the pO_2 in the tumor periphery responds to FiO_2 fluctuations, whereas the tumor core does not. The muscle has much higher pO_2 than either tumor region, which is especially apparent in the high-oxygen state.

The proposed method shows clear promise for imaging rapid oxygen changes *in vivo*, and warrants further exploration. A thorough experimental validation has not yet been performed, and would be a valuable future endeavor. It would also be useful to investigate other sources of pO_2 fluctuations, e.g., by performing resting-state imaging to measure spontaneous fluctuations in pO_2 rather than driven fluctuations. This would also provide an opportunity to evaluate the relationship between fluctuation source and model orders, i.e., to determine whether or not spontaneous fluctuations are as correlated as driven fluctuations.

Additional opportunities for technical development also remain, for example an improved scheme for selecting $\{c_{\ell mn}\}_{\ell=1,m=1,n=1}^{L,M,N}$ (which would allow construction of a stronger image model with even fewer degrees of freedom). Another area of technical development involves selection of the regularization term in Eq. (5), which was not explored in this work. This regularization term could be used to enforce additional complementary image properties, for example in the form of a weighted ℓ_2 penalty term or sparsity-promoting ℓ_1 penalty term. This would provide an avenue for exploiting additional signal properties [28] or for controlling model order [32, 42], at the expense of additional computational time.

CONCLUSIONS

We have described a new imaging scheme for fast oxygen imaging with EPRI. The proposed method is based on a low-rank tensor model that dictates a strategy for sparsely sampling (**k**, t, T_I)-space, as well as a particular image reconstruction algorithm. We have demonstrated the effectiveness of the method in simulations and *in vivo* experiments in tumor bearing mice with forced fluctuations in pO_2. Braun et al. [43] have demonstrated in a window chamber tumor model that oxygenation the frequency spectrum of tumor oxygenation changes diminishes at frequency below 1 Hz. The present imaging paradigm creates opportunities for noninvasively studying transient hypoxia and, in full three dimensional tumor models, assessing the extent to which tumor oxygenation changes. As highly localized animal radiation becomes available [44, 45], this will provide the first possibility for determining the clinical relevance of transient oxygen changes in mammalian tumors.

Acknowledgments

This work was supported by NIH grants P41 EB002034 and R01 CA098575.

REFERENCES

1. Overgaard J. Hypoxic radiosensitization: Adored and ignored. J Clin Oncol. 2007; 25:4066–4074. [PubMed: 17827455]
2. Schwarz G. Über Desensibilisierung gegen röntgen-und radiumstrahlen. Münchener Med Wochenschr. 1909; 56:1217–1218.

3. Al-Hallaq HA, Zamora M, Fish BL, Farrell A, Moulder JE, Karczmar GS. MRI measurements correctly predict the relative effects of tumor oxygenating agents on hypoxic fraction in rodent BA1112 tumors. Int J Radiat Oncol Biol Phys. 2000; 47:481–488. [PubMed: 10802376]
4. Hockel M, Schlenger K, Aral B, Mitze M, Schaffer U, Vaupel P. Association between tumor hypoxia and malignant progression in advanced cancer of the uterine cervix. Cancer Res. 1996; 56:4509–4515. [PubMed: 8813149]
5. Halpern HJ, Yu C, Peric M, Barth E, Grdina DJ, Teicher BA. Oxymetry deep in tissues with low-frequency electron paramagnetic resonance. Proc Natl Acad Sci U S A. 1994; 91:13047–13051. [PubMed: 7809170]
6. Thomlinson RH, Gray LH. The histological structure of some human lung cancers and the possible implications for radiotherapy. Brit J Radiol. 1955; 9:539–563.
7. Brown JM. Evidence for acutely hypoxic cells in mouse tumours, and a possible mechanism of reoxygenation. Brit J Radiol. 1979; 52:650–656. [PubMed: 486895]
8. Chaplin DJ, Olive PL, Durand RE. Intermittent blood flow in a murine tumor: Radiobiological effects. Cancer Res. 1987; 47:597–601. [PubMed: 3791244]
9. Trotter MJ, Chaplin DJ, Olive PL. Possible mechanisms for intermittent blood flow in the murine SCCVII carcinoma. Int J Radiat Biol. 1991; 60:139–146. [PubMed: 1677962]
10. Durand RE, Lepard NE. Contribution of transient blood flow to tumour hypoxia in mice. Acta Oncol. 1995; 34:317–323. [PubMed: 7779416]
11. Bayer C, Vaupel P. Acute versus chronic hypoxia in tumors: Controversial data concerning time frames and biological consequences. Strahlenther Onkol. 2012; 188:616–627. [PubMed: 22454045]
12. Elas M, Ahn KH, Parasca A, Barth ED, Lee D, Haney C, Halpern HJ. Electron paramagnetic resonance oxygen images correlate spatially and quantitatively with Oxylite oxygen measurements. Clin Cancer Res. 2006; 12:4209–4217. [PubMed: 16857793]
13. Epel B, Sundramoorthy SV, Mailer C, Halpern HJ. A versatile high speed 250-MHz pulse imager for biomedical applications. Concept Magn Reson B. 2008; 33B:163–176.
14. Elas M, Hleihel D, Barth ED, Haney CR, Ahn KH, Pelizzari CA, Epel B, Weichselbaum RR, Halpern HJ. Where it's at really matters: in situ in vivo vascular endothelial growth factor spatially correlates with electron paramagnetic resonance pO2 images in tumors of living mice. Mol Imaging Biol. 2011; 13:1107–1113. [PubMed: 20960236]
15. Epel B, Haney CR, Hleihel D, Wardrip C, Barth ED, Halpern HJ. Electron paramagnetic resonance oxygen imaging of a rabbit tumor using localized spin probe delivery. Med Phys. 2010; 37:2553–2559. [PubMed: 20632567]
16. Elas M, Parasca A, Grdina DJ, Halpern HJ. Oral administration is as effective as intraperitoneal administration of amifostine in decreasing nitroxide EPR signal decay in vivo. Biochim Biophys Acta Mol Basis Dis. 2003; 1637:151–155.
17. Mailer C, Sundramoorthy SV, Pelizzari CA, Halpern HJ. Spin echo spectroscopic electron paramagnetic resonance imaging. Magn Reson Med. 2006; 55:904–912. [PubMed: 16526015]
18. Epel, B.; Halpern, HJ. Proc IEEE Int Symp Biomed Imaging. Chicago, IL: IEEE; 2011. Comparison of transverse and spin-lattice relaxation based electron paramagnetic resonance oxygen images; p. 754-757.
19. Yasui H, Matsumoto S, Devasahayam N, Munasinghe JP, Choudhuri R, Saito K, Subramanian S, Mitchell JB, Krishna MC. Low-field magnetic resonance imaging to visualize chronic and cycling hypoxia in tumor-bearing mice. Cancer Res. 2010; 70:6427–6436. [PubMed: 20647318]
20. Subramanian S, Koscielniak JW, Devasahayam N, Pursley RH, Pohida TJ, Krishna MC. A new strategy for fast radiofrequency CW EPR imaging: Direct detection with rapid scan and rotating gradients. J Magn Reson. 2007; 186:212–219. [PubMed: 17350865]
21. Redler G, Epel B, Halpern HJ. Principal component analysis enhances SNR for dynamic electron paramagnetic resonance oxygen imaging of cycling hypoxia in vivo. Magn Reson Med. 2014; 71:440–450. [PubMed: 23401214]
22. Lustig, M.; Santos, JM.; Donoho, DL.; Pauly, JM. Proc Int Soc Magn Reson Med. Seattle, WA: 2006. k-t SPARSE: High frame rate dynamic MRI exploiting spatio-temporal sparsity; p. 2420

23. Lustig M, Donoho D, Pauly JM. Sparse MRI: The application of compressed sensing for rapid MR imaging. Magn Reson Med. 2007; 58:1182–1195. [PubMed: 17969013]
24. Liang, Z-P. Proc IEEE Int Symp Biomed Imaging. Arlington, VA: 2007. Spatiotemporal imaging with partially separable functions; p. 988-991.
25. Haldar, JP.; Liang, Z-P. Proc IEEE Int Symp Biomed Imaging. Rotterdam: 2010. Spatiotemporal imaging with partially separable functions: A matrix recovery approach; p. 716-719.
26. Christodoulou, AG.; Liang, Z-P. Proc Int Soc Magn Reson Med. Toronto: 2015. 3D dynamic T1 mapping of the myocardium using a time-varying subspace; p. 2614
27. Lingala SG, Hu Y, DiBella E, Jacob M. Accelerated dynamic MRI exploiting sparsity and low-rank structure: k-t SLR. IEEE Trans Med Imaging. 2011; 30:1042–1054. [PubMed: 21292593]
28. Zhao B, Haldar JP, Christodoulou AG, Liang Z-P. Image reconstruction from highly undersampled (k,t)-space data with joint partial separability and sparsity constraints. IEEE Trans Med Imaging. 2012; 31:1809–1820. [PubMed: 22695345]
29. Johnson DH, Ahmad R, He G, Samouilov A, Zweier JL. Compressed sensing of spatial electron paramagnetic resonance imaging. Magn Reson Med. 2014; 72:893–901. [PubMed: 24123102]
30. Kolda TG, Bader BW. Tensor decompositions and applications. SIAM Rev. 2009; 51:455–500.
31. Trzasko, JD.; Manduca, A. Proc Int Soc Magn Reson Med. Salt Lake City, UT: 2013. A unified tensor regression framework for calibrationless dynamic, multichannel MRI reconstruction.
32. He J, Liu Q, Christodoulou AG, Ma C, Lam F, Liang Z-P. Accelerated high-dimensional MR imaging with sparse sampling using low-rank tensors. IEEE Trans Med Imaging. (in press).
33. Zhao B, Lam F, Liang Z-P. Model-based MR parameter mapping with sparsity constraints: parameter estimation and performance bounds. IEEE Trans Med Imaging. 2014; 33:1832–1844. [PubMed: 24833520]
34. Zhao B, Lu W, Hitchens TK, Lam F, Ho C, Liang Z-P. Accelerated MR parameter mapping with low-rank and sparsity constraints. Magn Reson Med. 2015; 74:489–498. [PubMed: 25163720]
35. Sundramoorthy SV, Epel B, Mailer C, Halpern HJ. A passive dual-circulator based transmit/receive switch for use with reflection resonators in pulse EPR. Concept Magn Reson B. 2009; 35B:133–138.
36. Quine RW, Tseytlin M, Eaton SS, Eaton GR. A very fast switched attenuator circuit for microwave and R.F. applications. Concept Magn Reson B. 2010; 37B:39–44.
37. Epel B, Gromov I, Stoll S, Schweiger A, Goldfarb D. Spectrometer manager: A versatile control software for pulse EPR spectrometers. Concept Magn Reson B. 2005; 26B:36–45.
38. Epel B, Bowman MK, Mailer C, Halpern HJ. Absolute oxygen R1e imaging in vivo with pulse electron paramagnetic resonance. Magn Reson Med. 2014; 72:362–368. [PubMed: 24006331]
39. Redler G, Epel B, Halpern HJ. Maximally spaced projection sequencing in electron paramagnetic resonance imaging. Concept Magn Reson B. 2015; 45:33–45.
40. Haney CR, Fan X, Parasca AD, Karczmar GS, Halpern HJ, Pelizzari CA. Immobilization using dental material casts facilitates accurate serial and multimodality small animal imaging. Concept Magn Reson B. 2008; 33B:138–144.
41. Kruuv J, Inch W, McCredie J. Blood flow and oxygenation of tumors in mice. I. Effects of breathing gases containing carbon dioxide at atmospheric pressure. Cancer. 1967; 20:51–59. [PubMed: 6016872]
42. Christodoulou AG, Zhang H, Zhao B, Hitchens TK, Ho C, Liang Z-P. High-resolution cardiovascular MRI by integrating parallel imaging with low-rank and sparse modeling. IEEE Trans Biomed Eng. 2013; 60:3083–3092. [PubMed: 23744657]
43. Braun RD, Lanzen JL, Dewhirst MW. Fourier analysis of fluctuations of oxygen tension and blood flow in R3230Ac tumors and muscle in rats. Am J Physiol. 1999; 277:H551–H568. [PubMed: 10444480]
44. Chow JC, Leung MK, Lindsay PE, Jaffray DA. Dosimetric variation due to the photon beam energy in the small-animal irradiation: a Monte Carlo study. Med Phys. 2010; 37:5322–5329. [PubMed: 21089767]

45. Newton J, Oldham M, Thomas A, Li Y, Adamovics J, Kirsch DG, Das S. Commissioning a small-field biological irradiator using point, 2D, and 3D dosimetry techniques. Med Phys. 2011; 38:6754–6762. [PubMed: 22149857]

Highlights

1. Accelerated EPR imaging method using a low-rank tensor model that dictates a specialized approach to both data acquisition and imaging reconstruction.
2. The method enables 3D oxygen imaging at a frame rate of 2 frames per minute.
3. *In vivo* mouse images depict relationship between FiO_2 and pO_2 in both muscle and tumor periphery, but constant pO_2 in tumor core.

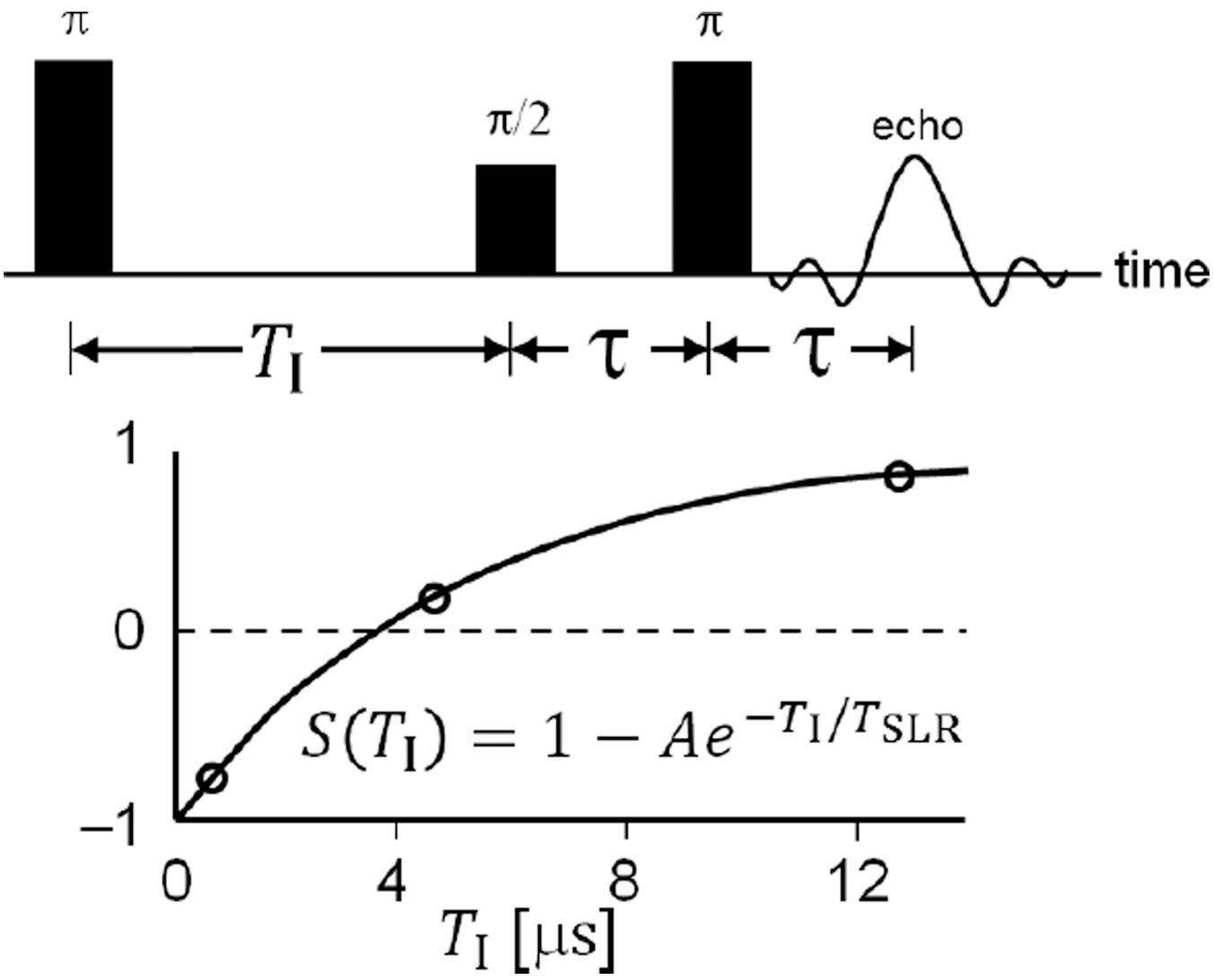

Figure 1.
Illustration of the IRESE pulse sequence used for data acquisition.

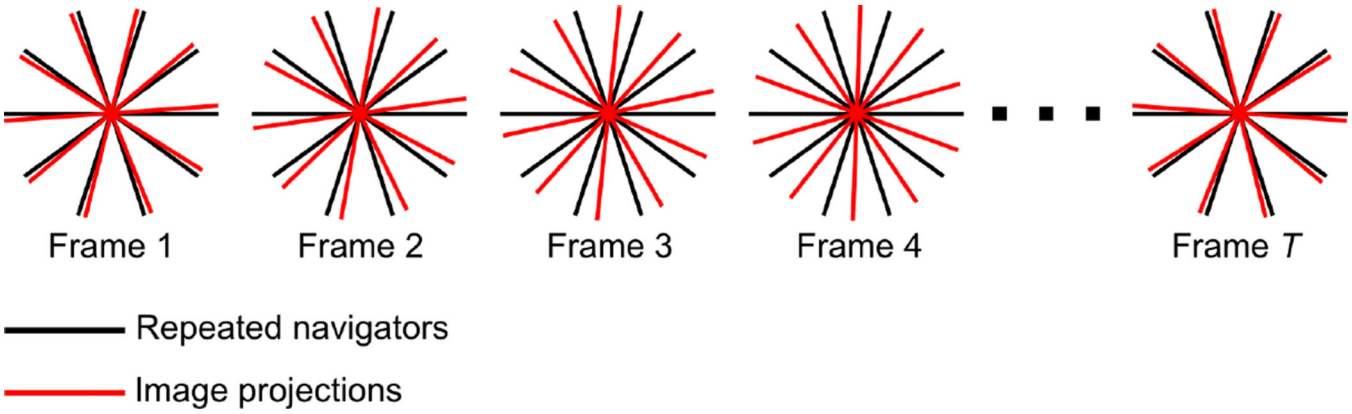

Figure 2.
Simplified 2D illustration of the sampling strategy used for data acquisition. The same navigator projections are acquired in each of the T frames, whereas the imaging projections change from frame-to-frame.

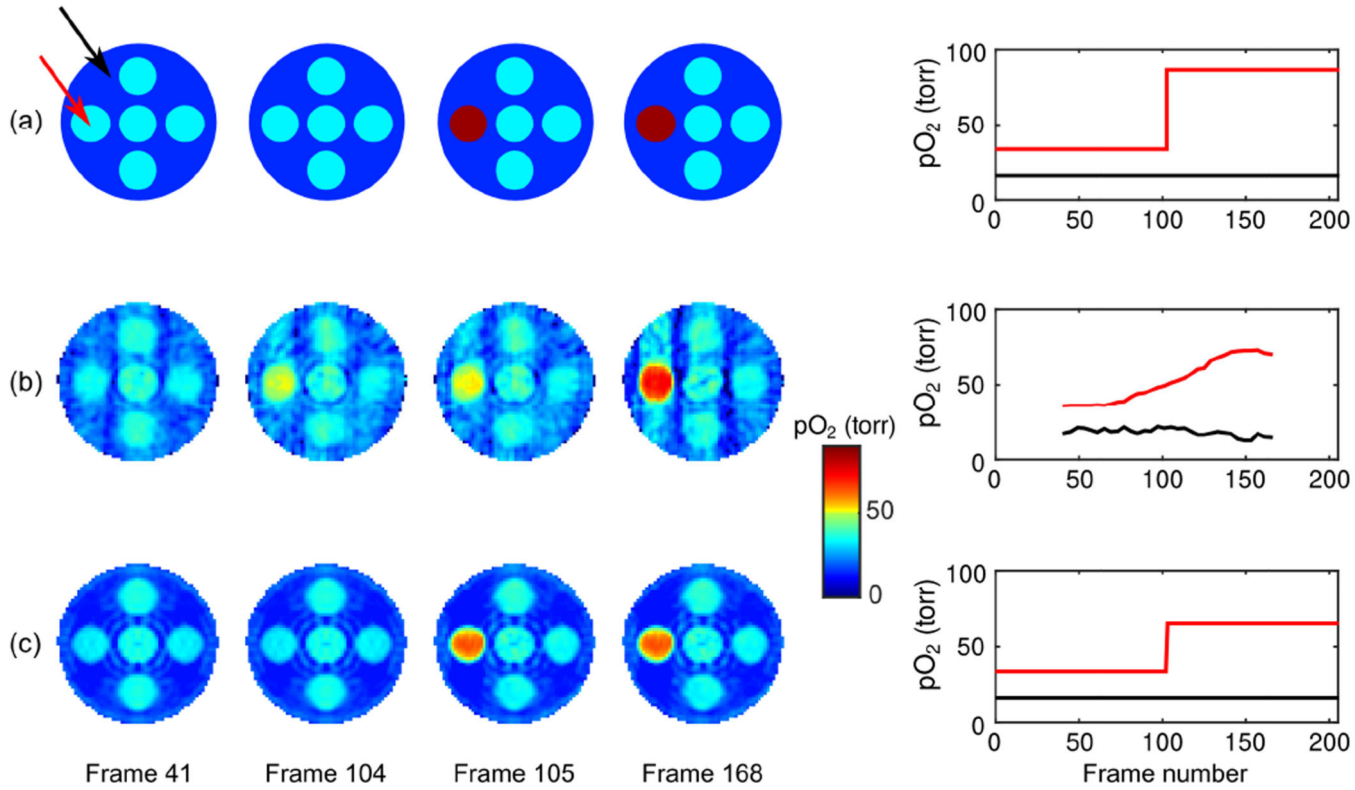

Figure 3.

Comparison of pO_2 maps and variation over time for (a) the analytical phantom, and for reconstructions using (b) conventional sliding window imaging and (c) the proposed low-rank tensor imaging method. pO_2 variation over time is shown for voxels in the dynamic sphere (red curve) and in the background sphere (black curve). The proposed method has greatly improved spatiotemporal fidelity, exhibiting reduced streaking artifacts and reduced temporal blurring.

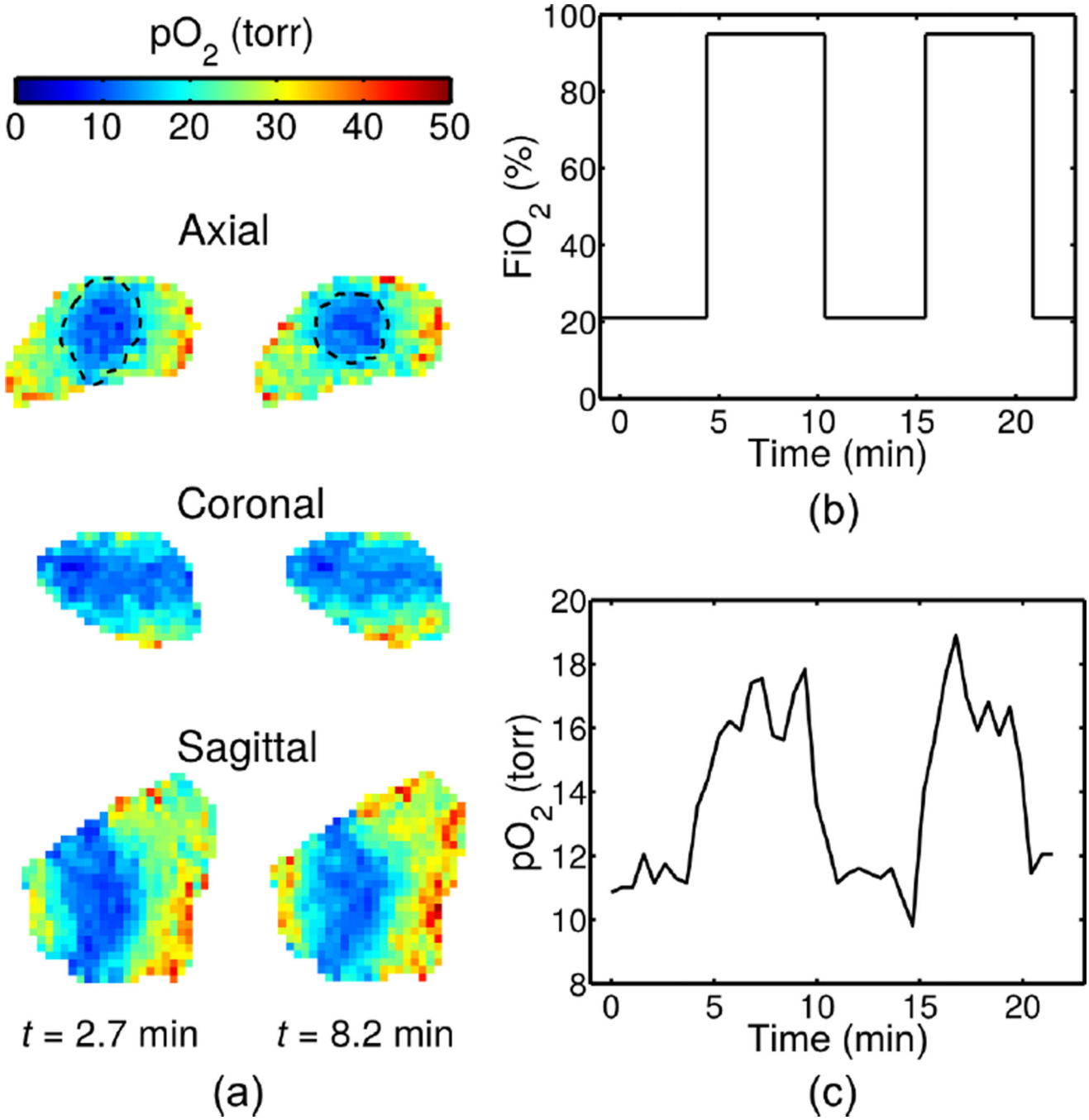

Figure 4.

(a) pO_2 maps at two time points, (b) FiO_2 inhaled by the mouse, and (c) variation over time at a voxel in the tumor periphery. The proposed method is capable of imaging at 2 frames/min, enabling detection of a clear, quick response of pO_2 to changes in FiO_2.

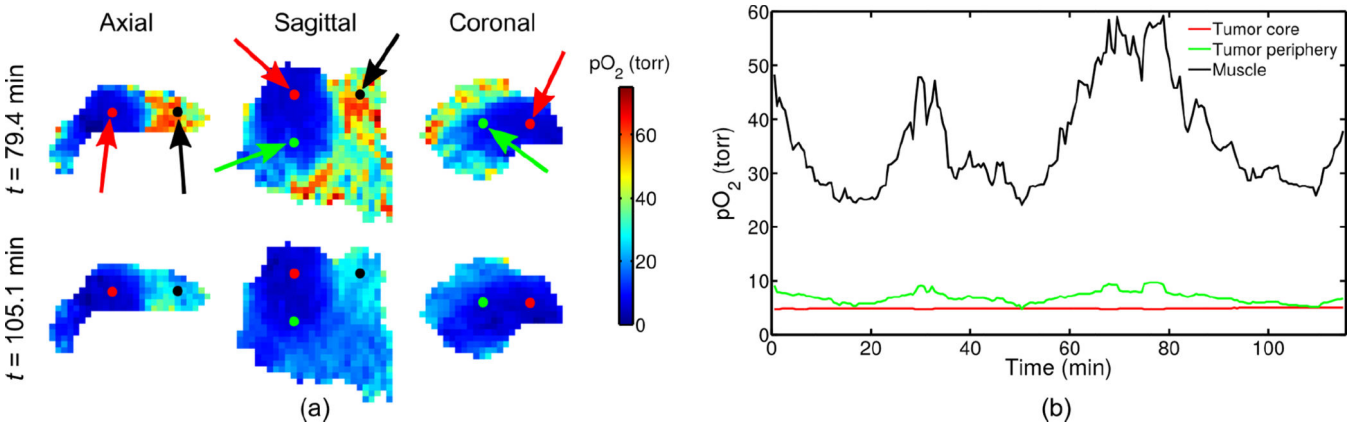

Figure 5.

(a) pO_2 maps at two time points and (b) variation over time at voxels of different tissue types (indicated by the colored arrows). Difference in pO_2 variations are clear in different parts of the tumor, allowing differentiation of the chronically hypoxic core of the tumor from the tumor periphery with higher vascular access.